

# Global resonance optimization analysis of nonlinear mechanical systems: Application to the uncertainty quantification problems in rotor dynamics

Haitao Liao \*

Chinese Aeronautical Establishment, Beijing 100012, China

## ARTICLE INFO

### Article history:

Received 9 July 2013

Received in revised form 13 February 2014

Accepted 17 February 2014

Available online 26 February 2014

### Keywords:

The worst resonant response

Multi-dimensional harmonic balance method

Quasi-Periodic Solution

The MultiStart algorithm

Uncertainty

## ABSTRACT

An efficient method to obtain the worst quasi-periodic vibration response of nonlinear dynamical systems with uncertainties is presented. Based on the multi-dimensional harmonic balance method, a constrained, nonlinear optimization problem with the nonlinear equality constraints is derived. The MultiStart optimization algorithm is then used to optimize the vibration response within the specified range of physical parameters. In order to illustrate the efficiency and ability of the proposed method, several numerical examples are illustrated. The proposed method is then applied to a rotor system with multiple frequency excitations (unbalance and support) under several physical parameters uncertainties. Numerical examples show that the proposed approach is valid and effective for analyzing strongly nonlinear vibration problems with different types of nonlinearities in the presence of uncertainties.

© 2014 Elsevier B.V. All rights reserved.

## 1. Introduction

The method of determining periodic solutions of nonlinear systems is one of the most important fields in nonlinear dynamics researches. Many approaches have been developed to approximate periodic solutions of nonlinear systems. The harmonic balance method (HBM) is a well-known method to obtain approximate periodic solutions of nonlinear differential equations by using a truncated Fourier series. Many variants on the HBM have emerged. For example, Cheung and Lau [1] proposed the incremental harmonic balance method. Cameron and Griffin [2] pioneered the development of the alternating frequency/time domain(AFT) method. Based on augmented Lagrangian to deal with nonsmooth contact-friction laws, Nacivet et al. [3] proposed the dynamic Lagrangian frequency-time (DLFT) method. This method has been successfully used to quantify the efficiency of friction ring dampers [4]. Hall et al. [5] developed an improved version of the HBM which is referred to as the high dimensional harmonic balance (HDHB) approach in this study. The HDHB method was successfully improved to investigate the aeroelastic motions of an airfoil in Ref. [6]. In the HDHB method, aliasing [7] can occur if nonlinearity introduces a higher harmonic order. LaBryer described this phenomenon in Ref. [8] and proposed filters to decrease aliasing. Cochelet et al. [9] presented another strategy for applying the classical HBM with a large number of harmonics. The basic idea consists in recasting the original system into a new system where nonlinearities are at most quadratic polynomials by introducing as many new variables as needed. Recently, a constrained harmonic balance method [10] which computes solutions for periodic autonomous systems has been proposed. In the constrained harmonic balance method, a

\* Tel.: +86 10 15810533731; fax: +86 010 84927669.

E-mail address: [ht0819@163.com](mailto:ht0819@163.com)

square system of nonlinear equations is generated by setting an unknown variable to a given value so that the size of the nonlinear algebraic equations is as many as unknowns. In order to estimate the number of selected harmonics for a given level of accuracy and reduce the size of the set of nonlinear algebraic equations, an adaptive harmonic balance method was developed in Ref. [11]. A global analysis method mixing a harmonic balance method and a homotopy technique is presented in Ref. [12] to find all the periodic solutions of a nonlinear system.

By making use of the harmonic balance method, a set of nonlinear algebraic equations is formed and is therefore well-determined. A nonlinear solver is then used to find zeros of such nonlinear equations. However, in order to perform parametric studies the nonlinear solver must be applied recursively. In addition, if the number of unknown variables is higher than the number of the nonlinear harmonic balance equations (such as structural parameters uncertainties), the nonlinear harmonic balance equations are the so called under-defined system which cannot be solved using the nonlinear root finding algorithm. Furthermore, the location of the nonlinear resonance extremum is a difficulty problem (see Page 1144 in Ref. [13]). Therefore, there is a need to locate the nonlinear resonance extremum and the nonlinear resonant frequency.

As mentioned previously, the harmonic balance method with a single fundamental frequency is limited to find periodic solutions and is unfit to find quasi-periodic solutions. The single-frequency harmonic balance method is therefore extended to the case where the solution is not periodic in time but is quasi-periodic. The first formal presentation of the harmonic balance method to obtain the quasi-periodic solutions of nonlinear systems is usually credited to Chua and Ushida [14]. Following the pioneer work of Chua and Ushida [14] in electronics, a similar approach named the incremental harmonic balance method with multiple time scales was reported by Lau et al. [15] and it was further developed in Ref. [16] to handle general multi-degree of freedom externally excited and autonomous dynamical systems with cubic nonlinearities. By utilizing the AFT method in conjunction with multi-frequency Fourier transforms, the multi-dimensional harmonic balance method (MHBM) was proposed in Ref. [17][18] to study the internal resonant vibrations of a nonlinear Jeffcott rotor with contact terms. In Ref. [19] the multi-dimensional harmonic balance method with arc-length continuation was extended to the nonlinear vibration analysis of a modified Jeffcott rotor with piece-wise radial stiffness. Based on the approximation of the frequency basis by a mono-dimensional one, a new methodology called the adjusted harmonic balance method has been introduced in Ref. [20].

Most structural and mechanical systems are subject to variability and uncertainty in real life. Thus, the performance characteristics of such systems are also subject to uncertainties. In structural dynamics, taking into account uncertainty is important for various reasons: to increase the robustness of design, to ensure the compliance of vibration levels to standards, to assess worst case behavior and so on. In many instances, simulating solutions using a deterministic model may lead to inaccurate computational results. Therefore, any realistic analysis of nonlinear systems must take the uncertainties into account. The uncertainty analysis of nonlinear systems has received considerable attention. The Monte Carlo simulation (MCS) is a standard technique which has been widely used in engineering community for stochastic simulations. However, MCS requires a tremendous computational cost.

There is a growing interest to develop efficient computational algorithms for uncertainty investigations in nonlinear systems. Different computational methodologies have been developed to quantify the uncertain response of nonlinear systems subject to parametric variability. The uncertainty in nonlinear systems can be modeled using probabilistic, interval or other methods. When the uncertain parameters are described as random variables with known probability distributions, the probabilistic methods can be used. In recent years, polynomial chaos expansion, which helps to describe random functions with convergent polynomial functions series in some independent random variables with joint density functions, has been applied to many engineering problems taking into account the effects due to uncertainty. In Refs. [21,22], the polynomial chaos expansion with the harmonic balance method is presented and applied to predict the dynamic behaviors in uncertain rotor systems with faults. By incorporating the polynomial chaos expansion with the multi-dimensional harmonic balance method, Didier [23] developed the Stochastic multi-dimensional harmonic balance method. Unfortunately, the probabilistic approaches require a wealth of data, often unavailable, to define the probability density function of the uncertain structural parameters. Furthermore, Millman et al. [24] found that the PCE fail to predict limit cycle oscillations.

In many real situations, the maximum possible ranges of variations expressed in terms of percentage of the corresponding nominal of the parameters are only known and can be modeled as uncertain but bounded type parameters. In such cases, the interval analysis method [25] is a viable alternative. However, the interval analysis often leads to an overestimation of the interval width [26]. Hence, reducing the overestimation in the interval method is a crucial issue to a successful interval analysis. To overcome these limitations, the objective of the present work is to develop a systematic methodology to determine the quasi-periodic solutions of nonlinear systems in the presence of uncertainty.

Remainder of this paper is organized as follows: the general formulation of the proposed method for determining the quasi-periodic solutions is presented in Section 2. Examinations of the proposed method using a rotor system are then conducted in Section 3. Finally, concluding remarks are presented and discussed in Section 4.

## 2. The proposed method

A method named constrained optimization multi-dimensional harmonic balance method (COMHBM) which combines the multi-dimensional harmonic balance method and the MultiStart optimization algorithm is proposed in this section. The proposed method is formulated as a constrained, nonlinear optimization problem. This paper is devoted to study the

worst resonant quasi-periodic response in nonlinear structure. Therefore, the maximum vibration response expressed by the norm of the Fourier coefficient can be set as the optimization objective of the nonlinear optimization problem.

Within the framework of nonlinear constraints optimization theory, the nonlinear algebraic equations derived from the multi-dimensional harmonic balance method are treated as the generally nonlinear equality constraints. With the nonlinear equality constraints, the MultiStart algorithm is selected to find the worst resonant quasi-periodic response of nonlinear systems. The proposed method is the first to consider the multi-dimensional harmonic balance nonlinear algebraic equations as the nonlinear equality constraints of the nonlinear constrained optimization problem.

## 2.1. The nonlinear equality constraints derived from the multi-dimensional harmonic balance method

To obtain the quasi-periodic solutions of nonlinear systems, the multi-dimensional harmonic balance method is adopted. To present the method, the following equation of motion with  $n$  degree of freedom is considered:

$$\mathbf{M}\ddot{\mathbf{u}} + \mathbf{D}\dot{\mathbf{u}} + \mathbf{K}\mathbf{u} + \mathbf{f}_{nl}(\mathbf{u}, \dot{\mathbf{u}}, t) = \mathbf{p}(t) \quad (1)$$

where  $\mathbf{M}$ ,  $\mathbf{C}$  and  $\mathbf{K}$  denote the mass, damping, and stiffness matrices,  $\mathbf{p}(t)$  stands for the time dependent external force,  $\mathbf{u}$ ,  $\dot{\mathbf{u}}$  and  $\ddot{\mathbf{u}}$  are respectively the displacement, velocity, acceleration vectors, and  $\mathbf{f}_{nl}(\mathbf{u}, \dot{\mathbf{u}}, t)$  means the nonlinear force.

In the multi-dimensional harmonic balance method, the unknown time function  $\mathbf{x}(t)$  can be written as a multiple Fourier series:

$$\mathbf{u}(t) = \sum_{\mathbf{k} \in \mathbb{Z}^M}^{\infty} [\mathbf{U}_k^c \cos(\mathbf{k}, \omega)t + \mathbf{U}_k^s \sin(\mathbf{k}, \omega)t] \quad (2)$$

where  $\mathbf{U}_k^c$  and  $\mathbf{U}_k^s$  are the Fourier coefficients vectors. The vector  $\omega = [\omega_1, \omega_2, \dots, \omega_M]$  is the incommensurable frequencies basis.  $\mathbf{k} = [k_1, \dots, k_M]$  with  $k_j = -N, -N+1, \dots, -1, 0, 1, \dots, N-1, N$  where  $N$  is the order of the Fourier series stands for the harmonic index combination vector and  $(.)$  represents the dot product

$$(\mathbf{k}, \omega)t = \sum_{i=1}^M k_i \omega_i t \quad (3)$$

In the present work, the following condition for retaining  $N$  harmonics is adopted[18]:

$$\sum_{i=1}^M |k_i| \leq N \quad (4)$$

which leads to the presence of  $N_H$  harmonic terms  $N_H = \frac{(2N+1)^M+1}{2}$ .

With the use of Eq. (4), substituting Eq. (2) into Eq. (1) and equating the coefficients of the harmonic terms yield the following nonlinear function:

$$\mathbf{g}(\mathbf{U}, \omega) = \mathbf{A}(\omega)\mathbf{U} - \mathbf{b}(\mathbf{U}, \omega) = \mathbf{0} \quad (5)$$

Where  $\mathbf{b} = [(\mathbf{C}_0)^T \ (\mathbf{C}_{k_1})^T \ (\mathbf{S}_{k_1}^c)^T \ \dots \ (\mathbf{C}_{k_j})^T \ (\mathbf{S}_{k_j}^s)^T \ \dots \ (\mathbf{C}_{k_{N_H}})^T \ (\mathbf{S}_{k_{N_H}}^s)^T]^T$  corresponds to the Fourier coefficients of the nonlinear forcing term and the external force;  $\mathbf{A}(\omega)$  and  $\mathbf{U}$  are respectively defined by

$$\begin{aligned} \mathbf{A} &= \text{diag} \left( \mathbf{K}, \begin{bmatrix} \mathbf{K} - (\mathbf{k}_1, \omega)^2 \mathbf{M} & (\mathbf{k}_1, \omega) \mathbf{D} \\ -(\mathbf{k}_1, \omega) \mathbf{D} & \mathbf{K} - (\mathbf{k}_1, \omega)^2 \mathbf{M} \end{bmatrix}, \dots, \begin{bmatrix} \mathbf{K} - (\mathbf{k}_j, \omega)^2 \mathbf{M} & (\mathbf{k}_j, \omega) \mathbf{D} \\ -(\mathbf{k}_j, \omega) \mathbf{D} & \mathbf{K} - (\mathbf{k}_j, \omega)^2 \mathbf{M} \end{bmatrix}, \dots, \begin{bmatrix} \mathbf{K} - (\mathbf{k}_{N_H}, \omega)^2 \mathbf{M} & (\mathbf{k}_{N_H}, \omega) \mathbf{D} \\ -(\mathbf{k}_{N_H}, \omega) \mathbf{D} & \mathbf{K} - (\mathbf{k}_{N_H}, \omega)^2 \mathbf{M} \end{bmatrix} \right) \\ \mathbf{U} &= [(\mathbf{U}_0)^T \ (\mathbf{U}_{k_1}^c)^T \ (\mathbf{U}_{k_1}^s)^T \ \dots \ (\mathbf{U}_{k_j}^c)^T \ (\mathbf{U}_{k_j}^s)^T \ \dots \ (\mathbf{U}_{k_{N_H}}^c)^T \ (\mathbf{U}_{k_{N_H}}^s)^T]^T \end{aligned} \quad (6)$$

The difficulty with solving Eq. (5) is in finding a relationship between  $\mathbf{b}(\mathbf{U}, \omega)$  and  $\mathbf{U}$  since the Fourier coefficients of the nonlinear forcing term are implicit functions of the Fourier coefficients of the displacement. To overcome this difficulty, the alternating frequency time technique [2] shown in Eq. (7) is employed.

$$\mathbf{U} \xrightarrow{\text{IFFT}^n} \mathbf{u}(t) \Rightarrow \mathbf{f}_{nl}(\mathbf{u}, \dot{\mathbf{u}}, t) \xrightarrow{\text{FFT}^n} \mathbf{b}(\mathbf{U}, \omega) \quad (7)$$

The key idea of the multi-dimensional harmonic balance method is to find the unknown harmonic coefficients  $\mathbf{U}$  in Eq. (5). As the conventional MHBM is used, Eq. (5) is a set of nonlinear equations being directly solved by a Newton-Raphson-type procedure. However, when the response of the nonlinear structure is desired over a range of frequencies, the solution of Eq. (5) must be repeated at each frequency. Furthermore, the application of the Newton-Raphson-type method requires that the number of unknown variables is equal to the number of nonlinear equations, that is, Eq. (5) is a well-defined nonlinear system. However, if the nonlinear system of algebraic equations is under-defined, which the number of the unknown variables is greater than the number of nonlinear equations in Eq. (5), the root finding algorithm can't be used to determine the unknown harmonic coefficients. Fortunately, quasi-periodic solution can be obtained in another

way once the nonlinear function of Eq. (5) is satisfied. Therefore, unlike the traditional implementations of the multi-dimensional harmonic balance method, the nonlinear function of Eq. (5) is used to construct the nonlinear equality constraints of optimization problem.

## 2.2. Optimization with GlobalSearch

As our objective of optimization is to find the optimal solution aiming to maximize the vibration response of the nonlinear system of Eq. (1), thus the nonlinear equality constraints of Eq. (5) have to be satisfied. Therefore, the following nonlinear optimization problem can be formulated:

$$\begin{aligned} f(\mathbf{x}) &= f(\mathbf{U}, \boldsymbol{\omega}, \boldsymbol{\nu}_u) = \max \|\mathbf{U}\|_2 \\ \text{s.t. } \mathbf{g}(\mathbf{x}) &= \mathbf{g}(\mathbf{U}, \boldsymbol{\omega}, \boldsymbol{\nu}_u) = \mathbf{A}(\boldsymbol{\omega}, \boldsymbol{\nu}_u)\mathbf{U} - \mathbf{b}(\boldsymbol{\omega}, \boldsymbol{\nu}_u) = 0 \end{aligned} \quad (8)$$

where  $\mathbf{x} = \{\mathbf{U}, \boldsymbol{\omega}, \boldsymbol{\nu}_u\}^T$ , the symbol  $\|\cdot\|$  denotes a vector norm and  $\boldsymbol{\nu}_u$  is a set of design parameters and/or uncertainty parameters.

The solution of this nonlinear optimization problem with respect to a vector of unknowns  $\mathbf{x} = \{\mathbf{U}, \boldsymbol{\omega}, \boldsymbol{\nu}_u\}^T$  gives a vector of Fourier coefficients  $\mathbf{U}^{opt}$  and a resonance frequency,  $\omega^{opt}$  at a set of parameter values  $\boldsymbol{\nu}_u^{opt}$ . Their accurate and effective calculation is a very important problem, which is discussed in the following section.

The choice of optimization algorithm is very important, because the final results are usually dependent on the specific algorithm in terms of accuracy and local minima sensitivity. In this investigation, the advanced OptQuest NonLinear Programs (OQNLP) MultiStart gradient-based algorithm from Ref. [27] along with the sequential quadratic programming (SQP) method [28,29] as the local solver is implemented and the gradients are approximated by finite differences.

A flowchart of the OQNLP MultiStart algorithm is shown in Fig. 1 in which SP( $xt$ ) stands for the starting point generator and  $xt$  represents the candidate starting point produced. Starting from the point  $xs$ , the local NLP solver  $L(xs; xf)$  produces the final point  $xf$ . The function UPDATE LOCALS( $xs; xf; w$ ) is then used to process and store solver output  $xf$  and the updated penalty weights,  $w$  is also calculated.

There are two stages of the algorithm. The algorithm performs  $n1, n2$  iterations for the stage1 and stage2, respectively. At each iteration, the starting point generator SP( $xt$ ) produces the candidate starting point  $xt$  and this point is also used to calculate the  $L1$  exact penalty value  $P(xt, w) = f(xt) + \sum_{i=1}^{(2N_f+1)n} w_i \cdot \text{viol}(g_i(xt))$  where  $w_i$  is the positive penalty weight and the function  $\text{viol}(g_i(xt))$  equals the absolute violation of the  $i$ th equality constraint of problem Eq. (8) at point  $xt$ . After finishing  $n1$  iterations in stage 1, the local solver  $L$  is called at the best point that has the smallest value of  $P$  in stage 1. In stage 2, the MultiStart algorithm runs the local solver  $L$  starting at the points that pass the distance and merit filters. For the distance filter, the distance factor distfactor is used to determine whether a point is in an existing basin of attraction. For the merit filter, the threshold factor threshfactor and waitcycle are used to update threshold. The basin radius of the distance filter and

```

Stage 1
Call L(x0, xf) (x0 = user initial point)
Call UPDATE LOCALS(x0, xf, w)
For i = 1: n1 Do
    Call SP(xt(i))
    Evaluate P(xt(i), w)
EndDo
xt* = point yielding best value of P(xt(i), w) over all stage one points (i = 1, 2, ..., n1).
call L(xt*, xf)
Call UPDATE LOCALS(xt*, xf, w)
threshold = P(xt*, w)

Stage 2
For i = 1: n2 Do
    Call SP(xt(i))
    Evaluate P(xt(i), w)
    Perform merit and distance filter tests:
    Call distance filter(xt(i), dstatus)
    Call merit filter(xt(i), threshold, mstatus)
    If (dstatus and mstatus = "accept") Then
        Call L(xt(i), xf)
        Call UPDATE LOCALS(xt(i), xf, w)
    EndIf
EndDo

```

**Fig. 1.** A flowchart of the OQNLP MultiStart algorithm.

the threshold of the merit filter are updated during the optimization process. A basin radius decreases after waitcycle consecutive start points. These two filters help the MultiStart algorithm to run with a few points and with high success rate. If the local solver  $L$  runs starting from the point that passes the distance and merit filters, it can yield a positive exit flag, which indicates convergence. A detailed analysis of the algorithm can be found in Ref. [27].

Optimization experiments for the selected nonlinear dynamical systems show that other optimization methods such as Generic Algorithm, Differential Evolution and Particle Swarm Optimization etc. fail to find the actual solution of Eq. (8) and the SQP method seems to be the best nonlinear programming method for the constrained optimization problem Eq. (8). It outperforms every other nonlinear programming method in terms of efficiency, accuracy, and percentage of successful solutions, over a large number of test problems. As for the MultiStart algorithm, the MultiStart algorithm owes much of its efficiency to its merit and distance filters and these two filters help the MultiStart algorithm to run the SQP method with a few starting points and high success rate. Therefore, the use of the MultiStart algorithm along with the SQP method is very important for finding the optimization solution of Eq. (8).

### 3. Application to select nonlinear dynamical systems

In order to demonstrate the effectiveness of the proposed method, three numerical examples which have been taken from recent publications [20,23,30] are considered.

#### 3.1. Duffing oscillator

##### 3.1.1. The model

A classical nonlinear Duffing oscillator which has been used extensively in the literature is used as the first example. The equation of motion for the Duffing oscillator is given by

$$\ddot{u} + 2\zeta\dot{u} + u + \gamma u^3 = f_1 \sin(\omega_1 t) + f_2 \sin(\omega_2 t) \quad (9)$$

where  $\zeta, \gamma$  are the damping coefficient and the nonlinear stiffness coefficient, respectively,  $f_1$  and  $f_2$  mean the force amplitudes.  $\omega_1$  and  $\omega_2$  are the two incommensurate excitation frequencies.

To align with the computational study in Ref. [20], the following structural parameters were chosen:  $\zeta = 0.1$ ,  $\gamma = 0.2$ ,  $f_1 = f_2 = 5$ ,  $\omega_1/\omega_2 = \sqrt{2}$ . The complete frequency response function shown in Fig. 2 was obtained over the entire frequency range [0,1,8] (rad/s) using an Arc-length continuation scheme, similar to that used in Ref. [20].

It can be seen from Fig. 2 that with a hardening spring ( $\gamma > 0$ ) the response curve tends to bend to the right and the system reaches the top amplitude at resonant peak  $P_{\max}$  of which the corresponding frequency is  $\omega_1 = 2.44$  (rad/s). Five quasi-periodic solutions of which the upper and lower response bounds are  $P_{\text{upp}}$  and  $P_{\text{low}}$  respectively coexist at the excitation frequency  $\omega_1 = 2.95$  (rad/s). In the following, two cases are investigated by utilizing the proposed method:

(1) Case 1: searching the resonant peak  $P_{\max}$ .

In order to obtain the resonant peak  $P_{\max}$ , the norm of Fourier coefficients  $\mathbf{U}$  is maximized. As explained previously, the unknown variables that have to be determined are the unknown Fourier coefficients  $\mathbf{U}$  and the frequency  $\omega_1$  of the quasi-periodic solution  $P_{\text{low}}$ .

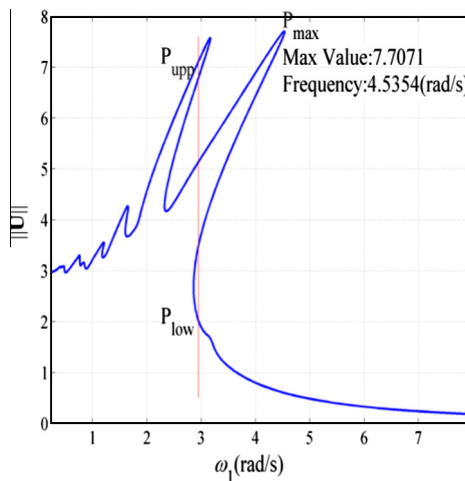


**Fig. 2.** Frequency-response curve of the Duffing oscillator with multi-harmonic forcing.

(2) Case 2: finding the upper and lower response bounds at a given frequency.

While looking for multiple solutions at a given frequency, the excitation frequency is not included as an optimization variable and the Fourier coefficients  $\mathbf{U}$  are the only unknown variables. It should be noted that the objective function in Eq. (8) is changed as the minimization of the norm  $\|\mathbf{U}\|$  for searching the quasi-periodic solution.

### 3.1.2. Numerical results

**3.1.2.1. Optimization results by the proposed method.** Based on the OQNLP MultiStart algorithm described in Section 2.2, optimizations are then performed to find these quasi-periodic solutions and the parameters of the optimization algorithm are listed as follows: Number of trial points was chosen to be 1000, and the usual value of 200 for the number of Stage1 points has been taken. The maximum number of generations allowed for the SQP algorithm was 600 while the function tolerance and the nonlinear equality constraints tolerance were both set to  $10^{-10}$ . A frequency range from 0.1 to 8 (rad/s) was considered. The number of harmonics retained  $N$  is 13 according to Ref. [20].

After the MultiStart algorithm stops successfully, numerical results are obtained. The optimization results are reported in Fig. 3 where the two dimensional time series are also plotted. The maximum values of the nonlinear equality constraints that were evaluated at these optimal solutions are  $1.3301e-11$  for  $P_{\max}$ ,  $4.2633e-13$  for  $P_{\text{upp}}$  and  $7.2374e-11$  for  $P_{\text{low}}$ , which are less than the nonlinear equality constraints tolerance  $10^{-10}$ . Therefore, the nonlinear algebraic equations in Eq. (5) are satisfied.

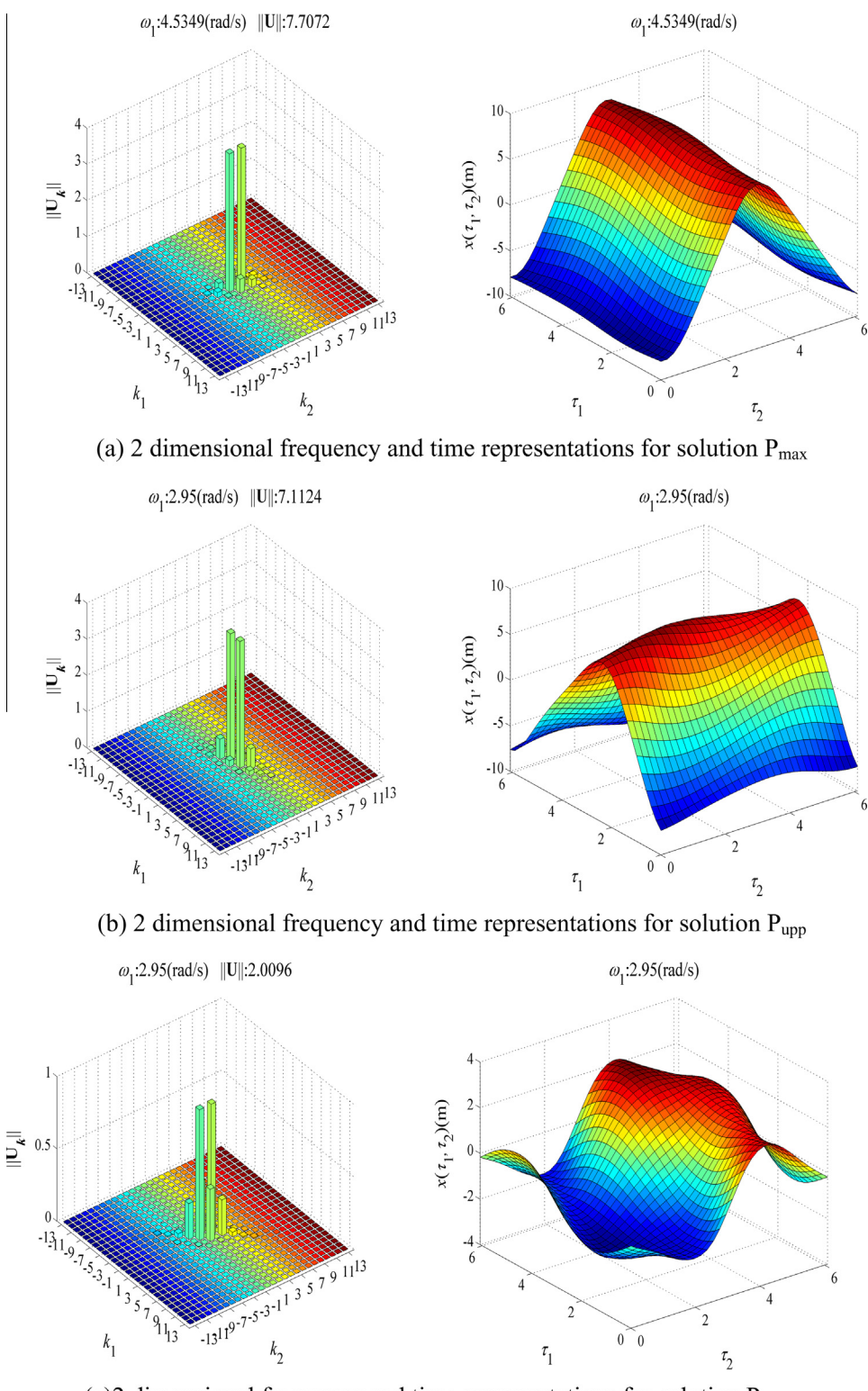
Observe in Fig. 3 that the maximum resonance peak found by the proposed method is 7.7072 at the nonlinear resonance frequency 4.5349 (rad/s). From Fig. 2 one can easily find that the resonance response level has its maximum value 7.7071 at the resonance frequency 4.5354 (rad/s). Comparison with Fig. 2 shows that the proposed method really finds the resonance peak. In addition, it can be seen from Fig. 3 that the presence of several harmonic components can be detected in the frequency spectrums and there is one main harmonic component in the system response. The solutions  $P_{\max}$  and  $P_{\text{low}}$  are dominated by the harmonic component  $[0, 1]$ , whilst the solution  $P_{\text{upp}}$  is dominated by the harmonic component  $[1, 0]$ . For  $P_{\text{low}}$ , the Duffing oscillator shows high magnitude oscillation not only at the harmonic component  $[0, 1]$ , rather it also exhibits harmonic response at the harmonic components  $[1, 0]$ ,  $[1, 2]$ , and  $[2, 3]$ . It should be noted that for calculating the quasi-periodic solutions  $P_{\text{upp}}$  and  $P_{\text{low}}$ , the proposed method can be viewed as a root finding algorithm.

**3.1.2.2. Comparison with numerical integration results.** In order to fully validate the proposed approach, direct numerical integrations have been performed. Numerical simulations are computed by the fourth order Runge–Kutta scheme with fixed step-size 0.001 here. The initial conditions can be readily supplied by the results of the presented method. In order to eliminate the transient part of the responses, the initial responses are discarded from the stored responses and results are plotted only for 900–1000. The time responses of the Duffing system at these optimal solutions using the time integration method and the proposed method are presented in Fig. 4 where the absolute errors between the two methods are also shown for these optimal solutions. The solid line and dashed line denote the proposed method solutions and the numerical integration results respectively.

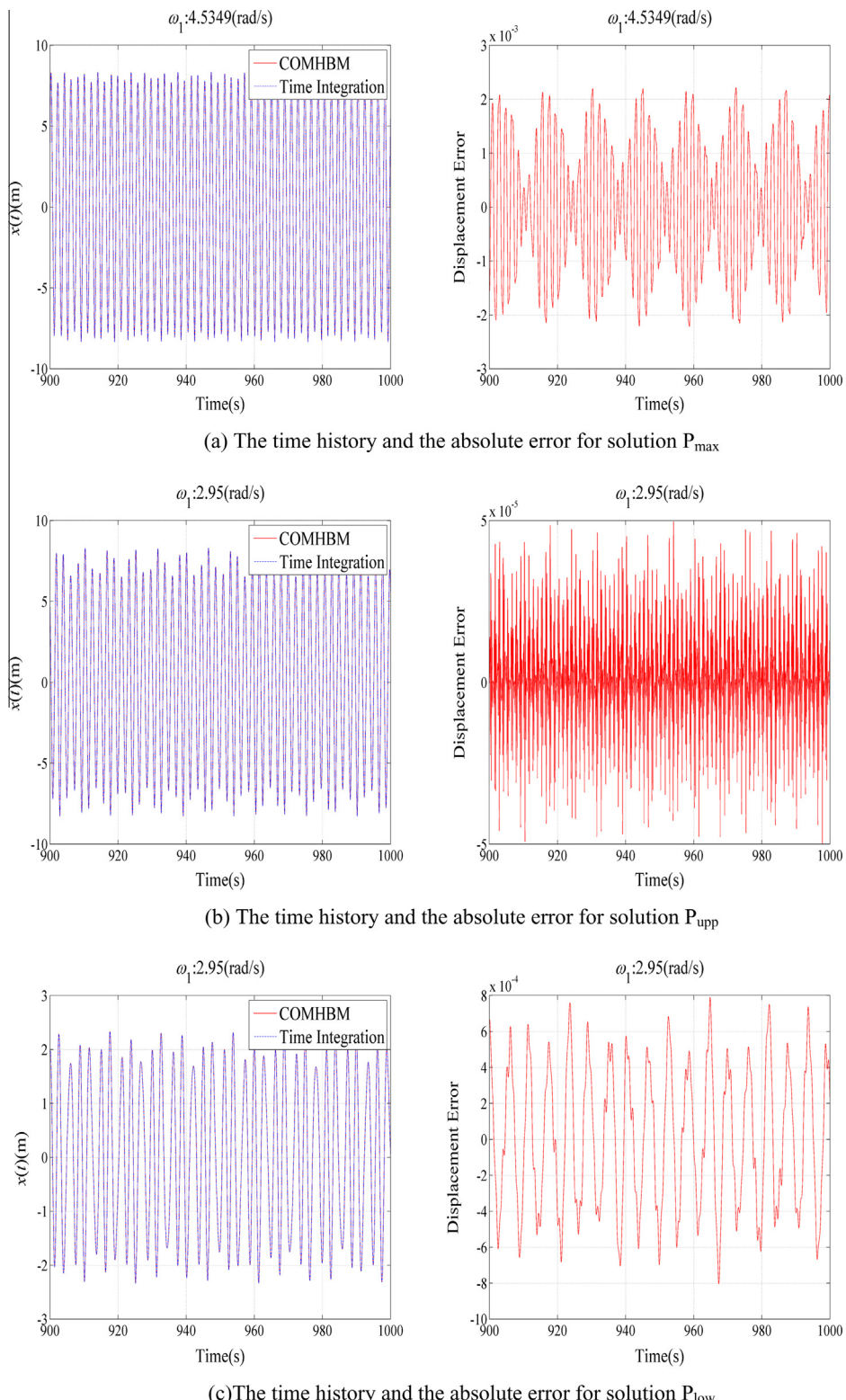
The results from the proposed method and from the time domain integration method are difficult to distinguish when they are plotted on the same graph. However, from the absolute errors in the time domain, the differences between numerical results from the proposed method and from the time integration method are clearly visible. Observe in Fig. 4 that there are small errors in amplitude and the maximum error corresponds to the resonant peak  $P_{\max}$ . For the resonant peak  $P_{\max}$  in Fig. 4, the maximum absolute difference between the responses as generated using the proposed method and the time integration method is less than  $3e-3$  while the maximum absolute displacement errors for solutions  $P_{\text{upp}}$  and  $P_{\text{low}}$  are less than  $5e-5$ ,  $8e-4$ , respectively. It is evident that the present approach solutions match well with the numerical integration solutions.

Fig. 5 shows the phase portraits and the corresponding frequency spectrums at these three solutions. As shown in Fig. 5, many loops are seen in the phase plane portrait and phase plane portraits are banded attractors. The phase orbits and the associated spectrums clearly indicate that the system is acting with quasi-periodic motions. For these solutions, there is one main harmonic terms in the system response and the presence of several harmonic components can be detected. For solution  $P_{\max}$ , the frequency spectrum is primarily composed of  $\omega_2$ , the influence of other harmonic components being insignificant. The largest peak for solution  $P_{\text{upp}}$  is detected at a non-dimensional frequency 1 while for solution  $P_{\text{low}}$ , the system vibrates with the dominate frequency  $\omega_2$  and a number of smaller peaks is observed. It can be seen from Figs. 4 and 5 that the proposed method is in excellent agreement with the time integration method both in time and frequency domains. The comparison between the proposed method and time integration method is extremely good.

The numerical simulations were performed on a Lenovo notebook computer with Intel Core processors i3-330 M of 2.13 GHz and 2 GB DDR3 RAM. For finding solutions  $P_{\max}$ ,  $P_{\text{upp}}$  and  $P_{\text{low}}$ , the proposed method requires 625.7813, 587.5313, 466.9063 s to converge while the CPU time required by the continuation method to calculate the frequency response curve in Fig. 2 is  $3.7542e3$  s. It is obvious that the CPU time needed by the proposed method to obtain the worst-case forced response is much less than that of the continuation method. The comparison of the computational cost shows the outstanding benefits that stem from the use of the present method.



**Fig. 3.** The optimization results obtained by the proposed method.



**Fig. 4.** The time series of the 3 quasi-periodic solutions using the proposed method and the time integration method and the absolute errors between the two methods.

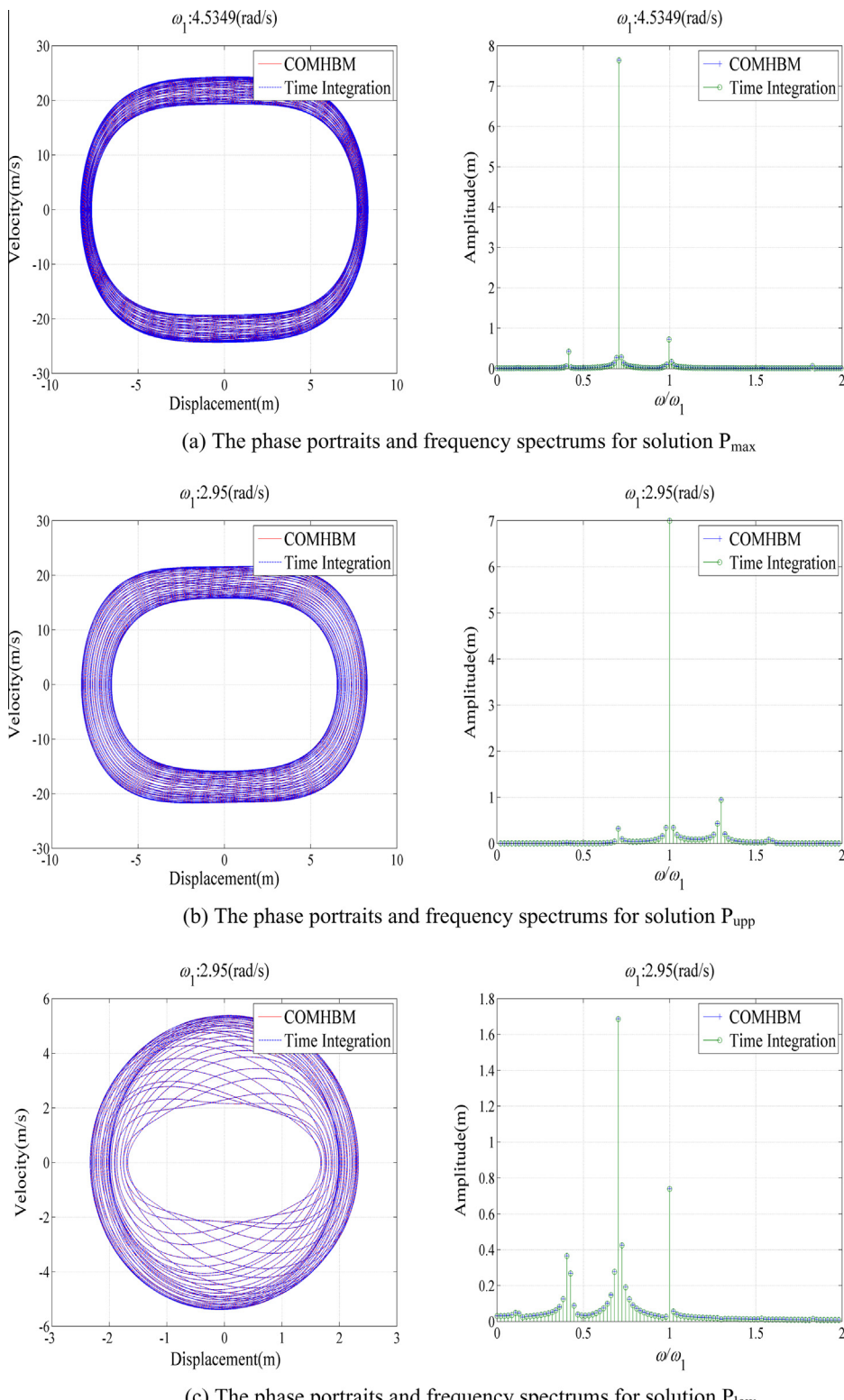


**Fig. 5.** The phase portraits and frequency spectrums of the 3 quasi-periodic solutions obtained by the proposed method and the time integration method.

### 3.2. A nonlinear two degree-of-freedom model with different types of nonlinearities and uncertainties

After the success of the proposed method in the above test model, the proposed method is applied to uncertainty quantification problems. The model considered in Ref. [23] is here chosen for the numerical simulations, as shown in Fig. 6.

#### 3.2.1. The nonlinear model

The system shown in Fig. 6 was studied in Ref. [23] to evaluate the performance of the multi-dimensional harmonic balance method with the polynomial chaos expansion. Structural nonlinearity is applied only in the first degree of freedom. The governing dynamic equations of the problem can be expressed as follows:

$$\begin{bmatrix} m & 0 \\ 0 & m \end{bmatrix} \begin{pmatrix} \ddot{u}_1 \\ \ddot{u}_2 \end{pmatrix} + \begin{bmatrix} 2c & -c \\ -c & 2c \end{bmatrix} \begin{pmatrix} \dot{u}_1 \\ \dot{u}_2 \end{pmatrix} + \begin{bmatrix} 2k & -k \\ -k & 2k \end{bmatrix} \begin{pmatrix} u_1 \\ u_2 \end{pmatrix} + \begin{pmatrix} f_{nl_1}(t) \\ 0 \end{pmatrix} = \begin{pmatrix} f_1 \cos(\omega_1 t) \\ f_2 \sin(\omega_2 t) \end{pmatrix} \quad (10)$$

where  $m$ ,  $c$ ,  $k$  are respectively the mass, damping coefficient and linear stiffness.  $f_{nl_1}(t)$  means the nonlinear force.  $f_1$  and  $f_2$  denote the forcing amplitudes.  $\omega_1$  and  $\omega_2$  represent the two incommensurable excitation frequencies with  $\omega_1/\omega_2 = \sqrt{2}$ .

In the following, two kinds of nonlinear force are considered

##### (1) Case 1: the contact force

The representation of the contact force is modeled as follows

$$f_{nl_1}(t) = \begin{cases} k_1 u_1(t), & \text{if } |u_1(t)| \leq u_{lim} \\ k_2 u_1(t) - sign(u_1(t))(k_2 - k_1)u_{lim}, & \text{if } |u_1(t)| > u_{lim} \end{cases} \quad (11)$$

where  $k_1$  and  $k_2$  define effective stiffness and  $u_{lim}$  represents the clearance value.

##### (2) Case 2: the friction force

The friction force  $f_{nl_1}(t)$  shown in Fig. 6(b) is represented as:

$$f_{nl_1}(t) = \begin{cases} k_f(u_1(t) - z(t)), & \text{if } |u_1(t)| \leq \mu P \\ \mu P sign(\dot{z}(t)), & \text{if } |u_1(t)| > \mu P \end{cases} \quad (12)$$

where  $k_f$  denotes the contact stiffness,  $\mu$  stands for the friction coefficient,  $P$  is the normal pressure and  $z(t)$  is the relative displacement of the contact point.

The deterministic system parameters for the model in Fig. 6 are listed in Table 1 where  $\bar{k}$  and  $\bar{\mu}$  are respectively the deterministic values of  $k$  and  $\mu$ , which is borrowed from Ref. [23]. The first-order and second-order natural frequencies of the underlying linear system are  $f_1 = 19.4924$  (Hz) and  $f_2 = 33.7619$  (Hz), respectively.

#### 3.2.2. Parameter uncertainties considered

In the following, the combined effects of parameter uncertainties and nonlinearities on the peak vibration response are investigated using the proposed method. Two cases of uncertainty with two external incommensurable frequencies  $\omega_1$  and  $\omega_2$  are considered. The excitation types applied to the model in Fig. 6 are the same as cases 6 and 7 in Ref. [23].

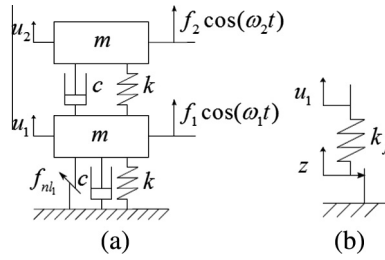


**Fig. 6.** The nonlinear model.

**Table 1**

Physical parameters of the system.

Parameter	$\bar{k}$	$m$	$c$	$f_1$	$f_2$	$k_1$	$k_2$	$k_f$	$\bar{\mu}$	$P$
Value (Unit)	15,000 (N m <sup>-1</sup> )	1 (kg)	1 (N m <sup>-1</sup> s <sup>-1</sup> )	1 (N)	1 (N)	$5 \times 10^{-4}$ (N m <sup>-1</sup> )	$5 \times 10^3$ (N m <sup>-1</sup> )	3000 (N m <sup>-1</sup> )	0.4	10 (N)

(1) Case1: uncertainty in the linear stiffness with the nonlinear contact force

A detuning parameter  $v_u \in [0, 1]$  with the small parameter  $\xi_k$  is introduced to quantify the deviation of  $k$  from the linear stiffness  $\bar{k}$ , and  $k(v_u)$  is described by

$$k = (1 - \xi_k + 2\xi_k * v_u)\bar{k} \quad (13)$$

with  $\xi_k = 0.05$ .

(2) Case2: uncertainty in the friction coefficient

The parameter uncertainty is modeled as a variation in the friction coefficient as:

$$\mu = (1 - \xi_\mu + 2\xi_\mu * v_u)\bar{\mu} \quad (14)$$

with  $\xi_\mu = 0.025$ ,  $v_u$  varies from 0 to 1.

### 3.2.3. Numerical results

**3.2.3.1. Optimization results of the worst-case resonance response.** Consider the optimization problem Eq. (8), the objective function to be optimized is the norm of the Fourier coefficients  $\mathbf{U}$ . Aiming at a maximization of the norm of the Fourier coefficients  $\mathbf{U}$ , the uncertainty variable  $v_u$  should be treated as optimization variable in the optimization problem of Eq. (8). Therefore, there are three categories of optimization variables including the uncertainty variable  $v_u$ , the unknown Fourier coefficients  $\mathbf{U}$  and the excitation frequency  $\omega_1$ . The approximation with one harmonic provides quite an accurate solution according to Ref. [23] and will be used in the rest of this paper. Optimizations are performed using the settings of the optimization algorithm similar to the first example. The optimization results for both cases are shown in Table 2 where also shows the worst resonance peaks of the deterministic systems. The nonlinear equality constraints that were evaluated at these optimization solutions are given in Table 2 where  $\max(|\mathbf{g}(\mathbf{U}, \boldsymbol{\omega}, \mathbf{v}_u)|)$  stands for the maximum absolute error of the multi-dimensional harmonic balance equations Eq. (5).

As can be seen from Table 2, for both cases the quasi-periodic responses are dominated by the harmonic component  $\mathbf{U}_{(0,1)}^c$  and the nonlinear equality constraints are satisfied. For case 1, a maximum norm of 5.8266e–3 was produced by the worst uncertain system at an excitation frequency of 28.6543 (Hz) while a maximum norm of 5.7633e–3 was experienced by the deterministic system at an excitation frequency of 28.9857 (Hz). It is observed that the resonance frequency corresponding to the worst uncertain system is lower than that of the deterministic system and the norm  $\|\mathbf{U}\|$  for case 1 changes a little at most when  $v_u$  varies. The response for case 1 is at its maximum when  $v_u = 0$ . The worst resonance response comparison for case 1 leads to the conclusion that a lower linear stiff  $k$  yields a larger vibration response.

On the contrary, for case 2 the optimization results of the worst uncertain system are very much identical with that of the deterministic system and the value of the resonant peak and the resonant frequency do not change. The uncertainty of the friction coefficient does not affect the norm of the Fourier coefficients  $\mathbf{U}$ . The worst resonance frequencies of the associated bi-periodic excitation are 27.5660, which is equal to  $\sqrt{2}\omega_1$ .

The phase portraits and the nonlinear forces associated with these optimization solutions are illustrated in Fig. 7. As illustrated in Fig. 7, the phase plots for both cases are symmetric with respect to the coordinate line and the motions in phase space are ellipse. For case 1, the vibration responses of  $u_1$  are lower than that of  $u_2$  whilst for case 2 the trajectories on the phase plane for  $u_1$  and  $u_2$  are coincide with each other. In addition, classical hysteresis curves of the nonlinear force-displacement relationship can be observed in Fig. 7(c) and (d).

**Table 2**

The optimization results obtained by the proposed method.

		Case 1		Case 2	
		The deterministic system	The worst uncertain system	The deterministic system	The worst uncertain system
<b>U</b>	<b>U<sub>(0,0)</sub></b>	1.0308e–20 5.1539e–21	−6.7328e–20 −3.3664e–20	−4.3801e–9 −2.1900e–9	−4.3801e–9 −2.1900e–9
	<b>U<sub>(0,1)</sub><sup>c</sup></b>	−3.8405e–3 −4.2953e–3	−3.8679e–3 −4.3404e–3	−4.0823e–3 −4.0827e–3	−4.0823e–3 −4.0827e–3
<b>U<sub>(0,1)</sub><sup>s</sup></b>	<b>U<sub>(0,1)</sub><sup>s</sup></b>	5.8192e–5 9.4007e–5	2.3939e–4 2.9812e–4	1.2017e–8 3.3340e–5	1.2000e–8 3.3340e–5
	<b>U<sub>(1,0)</sub><sup>c</sup></b>	1.3832e–5 −6.5705e–5	1.4519e–5 −6.7337e–5	−3.2851e–8 −6.6632e–5	−3.2851e–8 −6.6632e–5
<b>U<sub>(1,0)</sub><sup>s</sup></b>	<b>U<sub>(1,0)</sub><sup>s</sup></b>	1.9757e–5 −1.0048e–6	2.06343e–6 −1.0478e–6	1.5384e–6 −4.6086e–7	1.5384e–6 −4.6086e–7
	$\omega_1$	28.9857	28.6543	27.5660	27.5660
$v_u$			0		1
$\max( \mathbf{g}(\mathbf{U}, \boldsymbol{\omega}, \mathbf{v}_u) )$		2.8422e–14	1.4864e–11	1.6395e–14	1.3548e–12
Objective function value		5.7633e–3	5.8266e–3	5.7740e–3	5.7740e–3

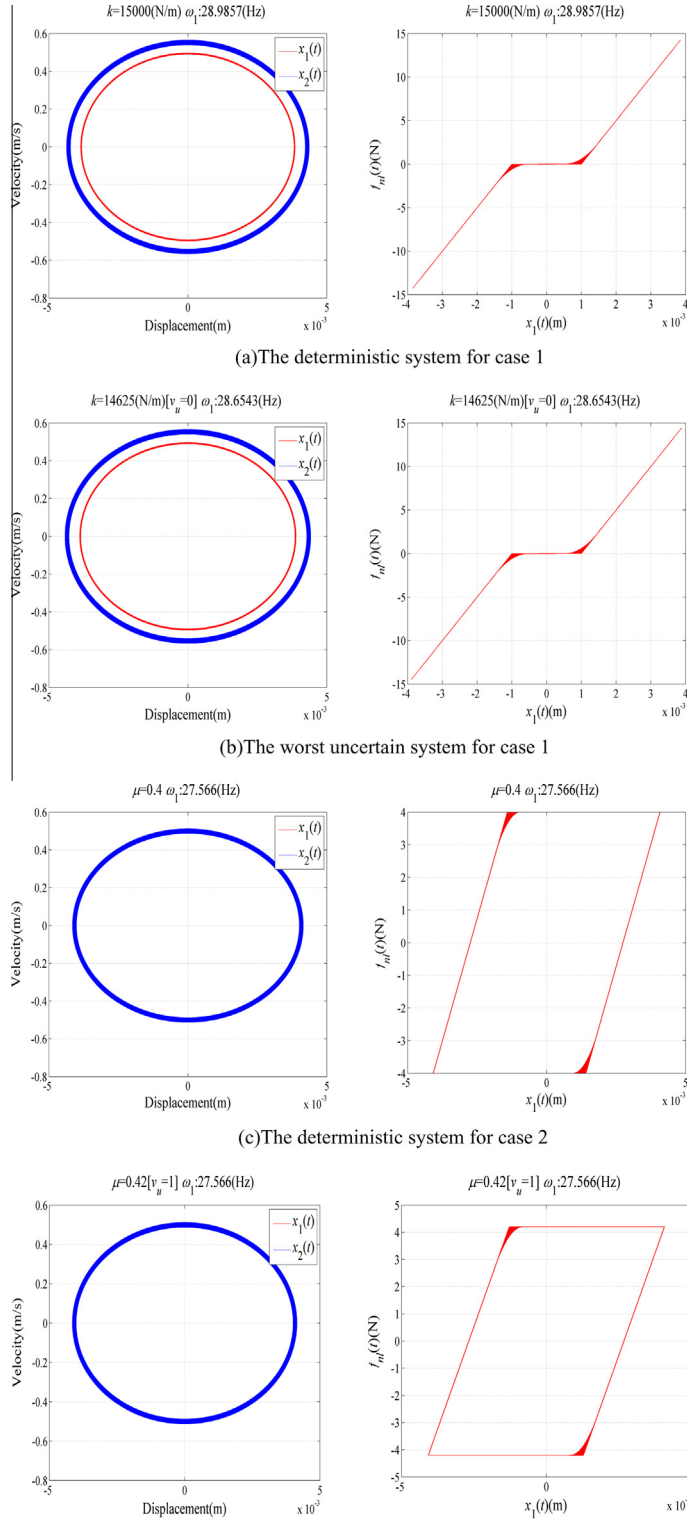


**Fig. 7.** The worst resonance phase portraits and force-displacement diagrams(cases a and b correspond to the deterministic system and the worst uncertain system for case 1, respectively while cases c and d represent, respectively the deterministic system and the worst uncertain system for case 2).

**3.2.3.2. Optimization results of the worst resonance response near the first natural frequency.** In order to study the nonlinear dynamics near the first natural frequency, the proposed method is again employed to predict the worst resonance responses. The variable  $v_u$  describing the uncertainty is the decision variable of the optimization problem. The excitation frequency variable is limited to the frequency range [18,22](Hz). All other parameters are the same as in the previous studies. The optimization results obtained by the presented method are illustrated in [Table 3](#).

As shown in [Table 3](#), it can be seen that the harmonic component  $\mathbf{U}_{(1,0)}^s$  dominates the quasi-periodic responses and the calculated worst resonance responses for both cases are slightly larger than the counterparts of the deterministic system. For case 1, a similar behavior has been found compared with the results in [Table 1](#). For case 2, a maximum norm 2.2355e–3 of the deterministic system is observed at a frequency of 20.3503 (Hz). On the other hand, the worst uncertain system has a peak response norm of 2.3253e–3 at an excitation frequency of 20.3558 (Hz). The resonance frequency corresponding to the worst uncertain system is higher than that of the deterministic system. Comparing the results between [Tables 2](#) and [3](#), it can be noted that for case 2 the nonlinearity only affects the dynamics of the resonance peak near the first natural frequency  $f_1$  whereas the dynamics of the worst resonance peak are not affected by the nonlinearity. In addition, it is interesting that the uncertainty values  $v_u$  for cases 1 and 2 are anomalously different. The vibration response for case 1 reaches the resonance peak of 5.2266e–3 when the coefficient of linear stiffness approaches its lower bound while the norm  $\|\mathbf{U}\|$  for case 2 takes its maximum when  $v_u = 1$ .

**3.2.3.3. The frequency response curves of the worst uncertain systems.** For comparison, forced responses of the worst resonant scenarios listed in [Tables 2](#) and [3](#) are also calculated as a function of excitation frequency using the multi-dimensional harmonic balance method with the continuation method. Frequency response curves are drawn in [Fig. 8](#) for case 1 and [Fig. 9](#) for case 2. In [Figs. 8 and 9](#), a zoom on the first two resonance peaks is done.

As can be seen in [Figs. 8 and 9](#), four main resonance peaks are observed and the peaks of the frequency response curves are sharp and narrow. As expected, the first two most important peaks are near the first natural frequency  $f_1$  of the underlying linear system. The response curves for case 1 show hardening-spring nonlinear characteristics and the resonant peaks of the worst uncertain system shift towards left slightly. The softening behavior of the system is confirmed in [Fig. 9](#). It is noted that for case 1 the resonant peaks of the worst uncertain system are slightly higher than the counterparts of the determined system while for case 2 the friction coefficient has no effect on the largest resonant peak. However, in the vicinity of the first resonant peak for case 2, discrepancy is observed but remains very small. Therefore, the results in [Tables 2 and 3](#) are validated by comparison with the conventional calculation of the forced response curves in [Figs. 8 and 9](#).

**3.2.3.4. Comparison with Monte Carlo simulation results.** The last part of this section is dedicated to the efficiency of the proposed method compared to Monte Carlo simulation. In Monte Carlo simulation, a series of quasi-periodic solutions can be obtained by taking all values over the considered bounded regions of  $v_u$ . With the aid of the attained solutions, the bounds and some properties of the quasi-periodic motions are determined and compared with the results in [Tables 2 and 3](#). [Fig. 10](#) shows the influences of the linear stiffness  $k$  and the friction coefficient  $\mu$  on the norm of  $\mathbf{U}$ . The curves shown in [Fig. 10](#) are obtained by taking the norm  $\|\mathbf{U}\|$  for all realizations at each  $v_u$ . For case 1, the norm  $\|\mathbf{U}\|$  for the first two resonant peaks varies very slowly with respect to  $v_u$  and it decreases monotonically when  $v_u$  increases from 0 to 1. Therefore, the norms of the previous two peaks are monotonically decreasing functions of linear stiffness  $k$ . For case 2, the norm  $\|\mathbf{U}\|$  for the second resonance peak remains the same while for the first resonance peak the norm  $\|\mathbf{U}\|$  increases monotonically with the increase of uncertainty. Therefore, the quasi-periodic solutions obtained by the proposed method are in good excellent agreement with the MCS results. Hence, the proposed method is utilizable.

**Table 3**  
The optimization results obtained by the proposed method.

		Case 1		Case 2	
		The deterministic system	The worst uncertain system	The deterministic system	The worst uncertain system
<b>U</b>	<b>U<sub>(0,0)</sub></b>	2.5344e–21	–4.1020e–21	–1.1588e–20	–4.9528e–21
		1.2672e–21	–2.0545e–21	–5.7938e–21	–2.4764e–21
	<b>U<sub>(0,1)</sub><sup>c</sup></b>	–5.1437e–7	–5.3150e–7	–8.7024e–7	–8.7173e–7
		–8.0961e–7	–8.4086e–7	–1.0702e–6	–1.0718e–6
<b>U<sub>(0,1)</sub><sup>s</sup></b>	<b>U<sub>(0,1)</sub><sup>s</sup></b>	4.4598e–5	4.5572e–5	5.9667e–5	5.9713e–5
		7.6740e–5	7.8667e–5	8.6821e–5	8.6870e–5
	<b>U<sub>(1,0)</sub><sup>c</sup></b>	1.1882e–4	1.1331e–4	–3.7701e–5	–3.8358e–5
		9.1777e–5	8.4793e–5	–5.8271e–5	–5.9730e–5
<b>U<sub>(1,0)</sub><sup>s</sup></b>	<b>U<sub>(1,0)</sub><sup>s</sup></b>	3.4599e–3	3.4873e–3	1.5026e–3	1.5625e–3
		3.8465e–3	3.8893e–3	1.6504e–3	1.7173e–3
$\omega_1$		20.4472	20.2163	20.3503	20.3558
$v_u$			0		1
max( g(U, $\omega$ , $v_u$ ) )		4.1545e–13	9.3234e–11	9.7367e–13	2.2138e–12
Objective function value		5.1765e–3	5.2266e–3	2.2355e–3	2.3253e–3

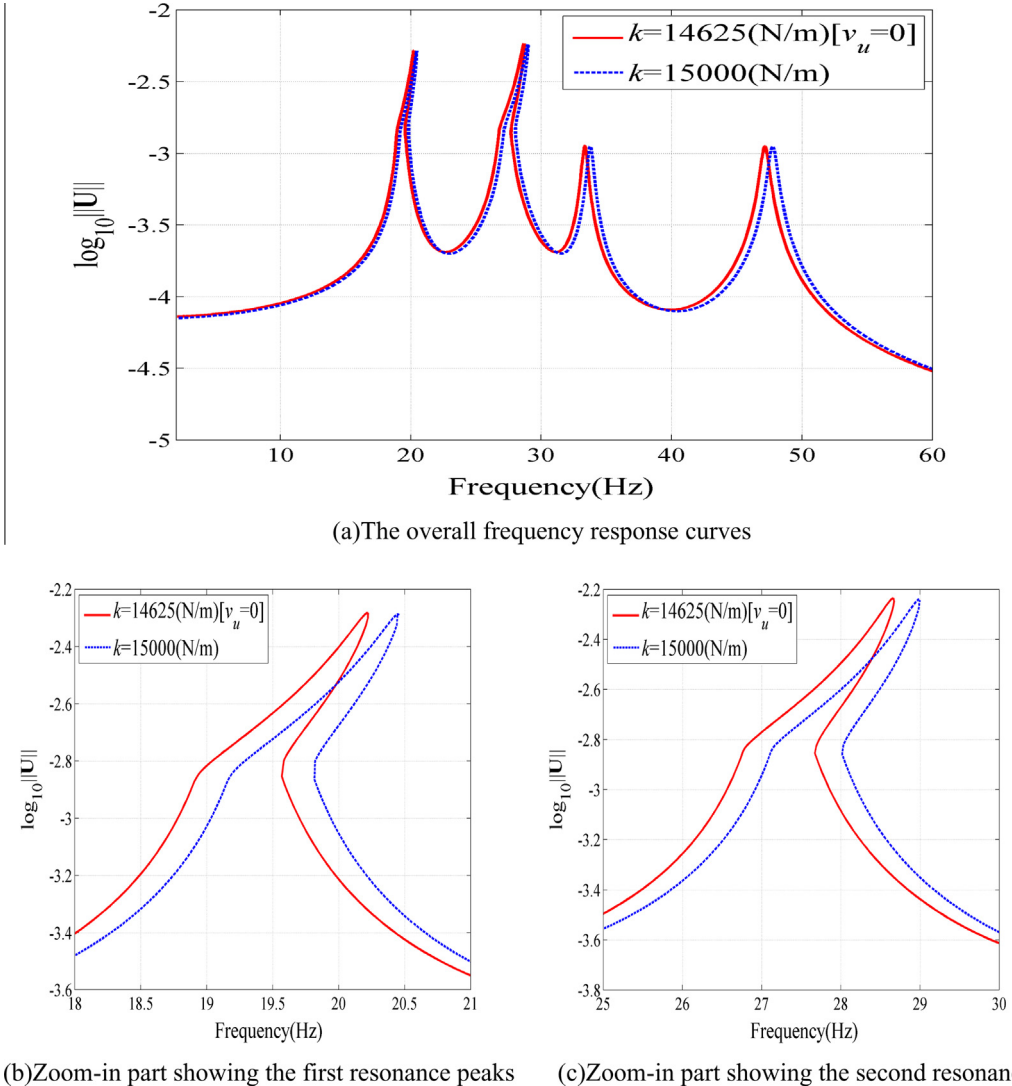


**Fig. 8.** The frequency response curves for case 1.

### 3.3. A finite element rotor model taking into accounts parameter uncertainties

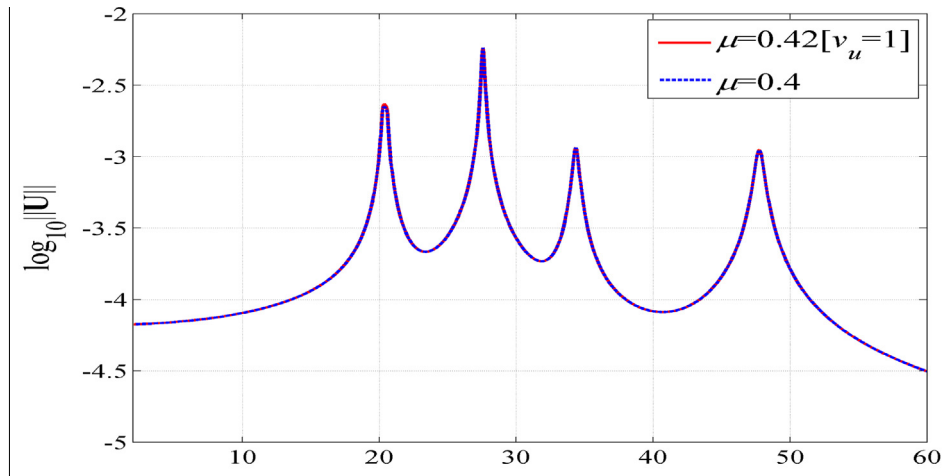
The third example considered is a finite element rotor model which is shown in Fig. 11. This example is borrow from Ref. [30]. As shown in Fig. 11, the rotor is divided into 10 Euler beam elements. At each node, four degrees of freedom including two translation displacements  $v, w$  and rotation angles  $\theta, \psi$  are considered. As illustrated in Fig. 11(b), two flats on the shaft are presented and the angle, the depth and the radius of the asymmetric section are denoted by  $\alpha, h, R$ . Therefore, the elements 3,4 and 5 are asymmetric. The rotor is simply supported at two ends. At the right bearing of the rotor system, a support excitation with a pulsation  $\omega_b$  is applied in the  $y$ -direction.

#### 3.3.1. The rotor model

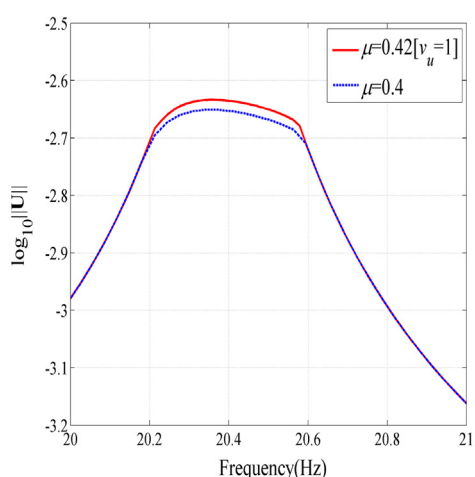
After derivation, the element matrices are obtained and listed in Appendix. It is note that the element matrices  $\mathbf{M}_0^e, \mathbf{K}_0^e, G^e$  are associated with  $I_m = (I_x + I_y)/2$  while  $\mathbf{M}_c^e, \mathbf{M}_s^e, \mathbf{K}_c^e, \mathbf{K}_s^e$  are function of  $I_d = (I_x - I_y)/2$ . For the asymmetry elements, the moments of inertia  $I_x$  and  $I_y$  are given by

$$\begin{aligned} I_x &= \frac{R^4}{2} \left( \alpha - \frac{\sin(2\alpha)}{2} \right) + \sqrt{2hR - h^2}(R-h)^3 \\ I_y &= \frac{R^4}{2} \left( \alpha + \frac{\sin(2\alpha)}{2} \right) + \frac{(2hR-h^2)^{3/2}}{3}(R-h) \end{aligned} \quad (15)$$

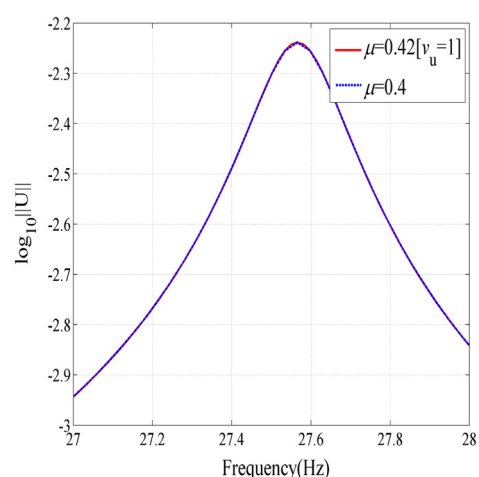
By assembling the shaft, disk and bearing elementary matrices, the governing dynamic equations of the rotor are expressed as follows:



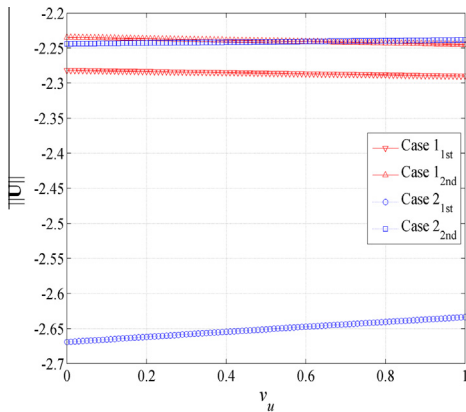
(a)The overall frequency response curves



(b)Zoom-in part showing the first resonance peaks



(c)Zoom-in part showing the second resonance peaks

**Fig. 9.** The frequency response curves for case 2.**Fig. 10.** The Monte Carlo simulation results.

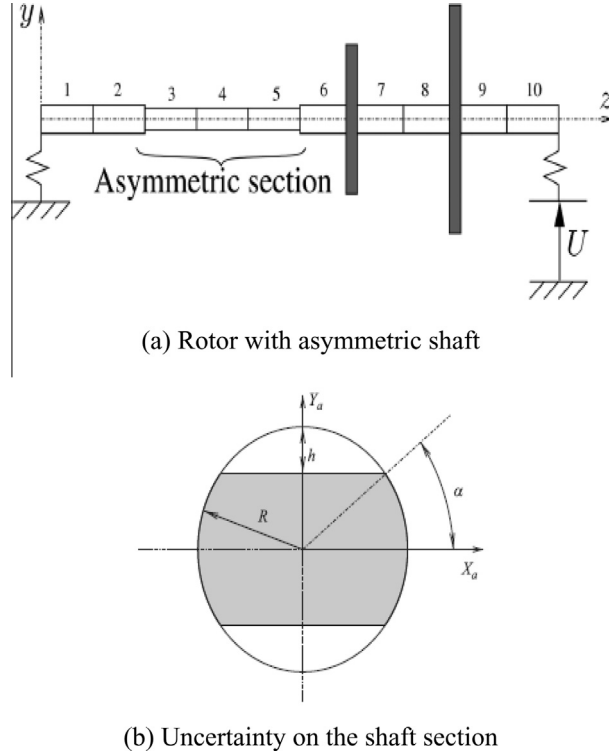


**Fig. 11.** The rotor model.

$$\mathbf{M}\ddot{\mathbf{u}} + (\mathbf{C} + \boldsymbol{\omega}_r\mathbf{G})\dot{\mathbf{u}} + \mathbf{K}\mathbf{u} = \mathbf{p}(t) \quad (16)$$

where  $\mathbf{M} = \mathbf{M}_0 + \mathbf{M}_c \cos(2\omega_r t) + \mathbf{M}_s \sin(2\omega_r t)$ ,  $\mathbf{K} = \mathbf{K}_0 + \mathbf{K}_c \cos(2\omega_r t) + \mathbf{K}_s \sin(2\omega_r t)$ ,  $\mathbf{C}$  and  $\mathbf{G}$  are the global mass, stiffness, damping and gyroscopic matrices and  $\omega_r$  represents the rotating speed of the rotor.  $\mathbf{p}(t)$  denotes the external force.

In the following, two kinds of external force are considered:

(1) Unbalance. By adding an unbalanced mass  $m_e$  with a distance  $d_e$  relative to the axis of rotation, the unbalance rotating force is given by:

$$\mathbf{p}^d = m_e d_e \omega_r^2 [\cos(\omega_r t) \quad \sin(\omega_r t) \quad 0 \quad 0]^T \quad (17)$$

(2) Excitation Support. The rotor base excitation force acting at the end of the shaft is modeled as follows:

$$\mathbf{p}^b = [0 \quad k_{yy} U_0 \cos(\omega_b t) \quad 0 \quad 0]^T \quad (18)$$

where  $k_{yy}$  means the bearing stiffness in the  $y$ -direction and  $U_0$  is the excitation amplitude.

**Table 4**  
Physical parameters of the rotor system.

Parameter	Dimension
Length of shaft	1 (m)
Diameter of shaft	0.04 (m)
Position of disc 1	0.6 (m)
Position of disc 2	0.8 (m)
Outer diameter of disc 1	0.2 (m)
Outer diameter of disc 2	0.4 (m)
Inner diameter of discs 1 and 2	0.04 (m)
Thickness of discs 1 and 2	0.02 (m)
Young modulus of elasticity E	$2.1e11$ ( $Nm^2$ )
Density	$7800$ ( $Kg m^{-3}$ )
Mass unbalance	0.05
Eccentricity of the mass unbalance	0.01
Depth of the asymmetry	0.002 m

**Table 5**

The parameter uncertainty bounds for the two cases.

Parameter	$\xi_E$ (%)	$\xi_{U_0}$ (%)	$\xi_m$ (%)	$\xi_h$ (%)
Case 1	5	5	–	–
Case 2	5	5	5	5

**Table 6**

The optimization results using the developed method.

Parameters	$\omega_r$	$\omega_b$	$v_E$	$v_{U_0}$	$v_m$	$v_h$
Case 0	3.4842	28.8661	–	–	–	–
Case 1	3.1483	28.5982	0	1	–	–
Case 2	3.2608	28.5884	0	1	1	1

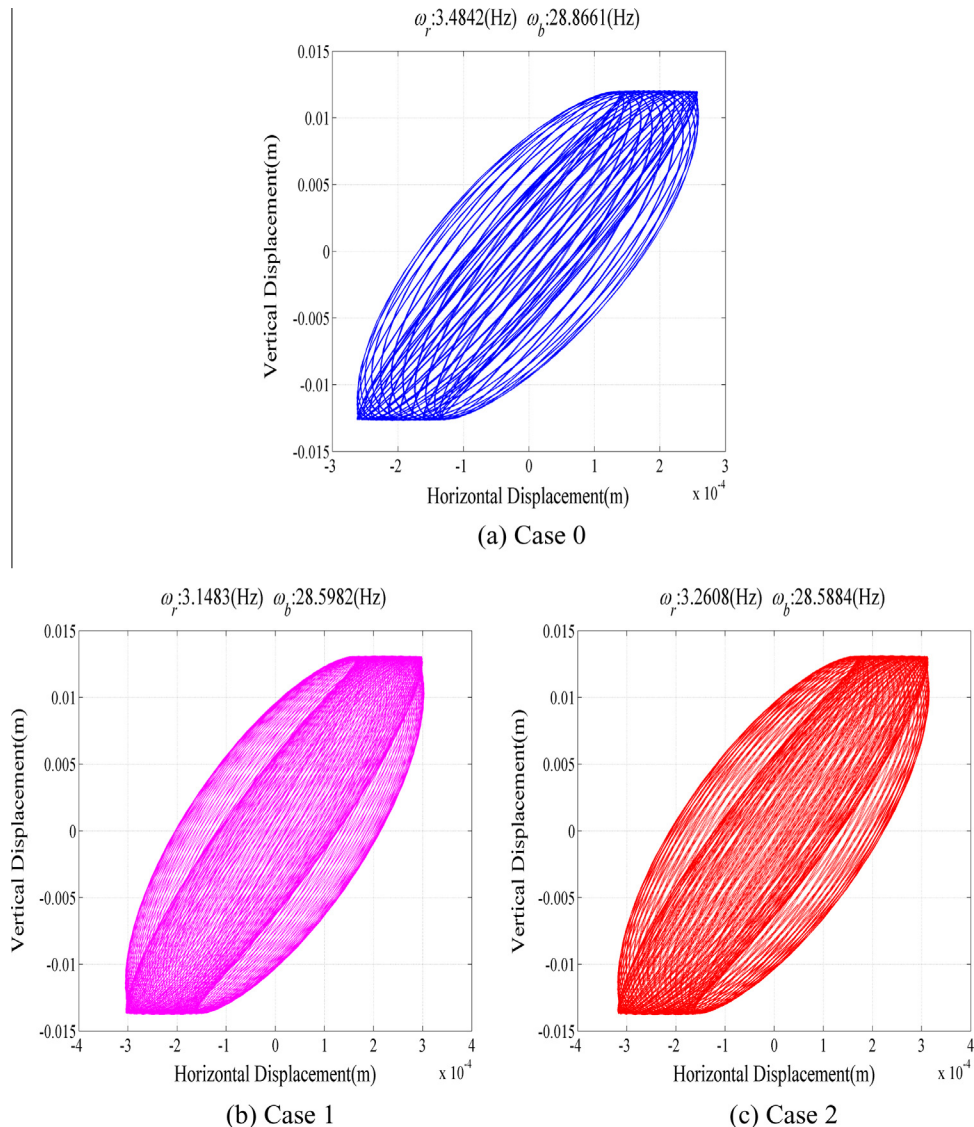


**Fig. 12.** The orbits of the rotor system at node 7 for the three cases.

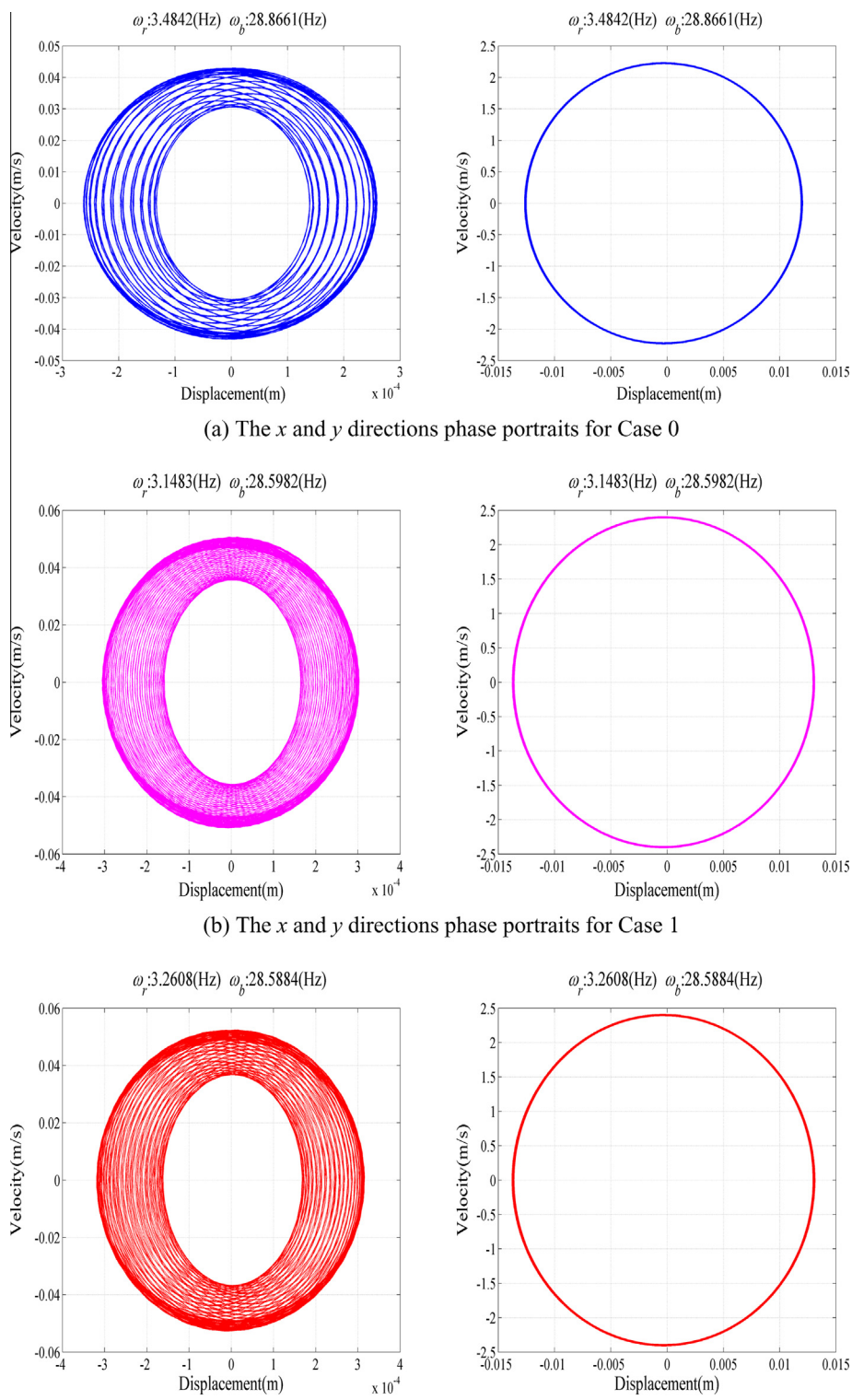


**Fig. 13.** The phase portraits of node 7 in the  $x$  and  $y$  directions for the three cases (The left figures represent the portraits in the  $x$  direction and the portraits in the  $y$  direction correspond to the right figures).

For the rotor system shown in Fig. 11, the rotor parameters are set to be the same with Ref. [30] and Table 4 lists the values of system parameters. The first, second and third critical speeds are around  $f_1 = 28.8$  (Hz),  $f_2 = 98.1$  (Hz) and  $f_3 = 174.5$  (Hz), respectively.

### 3.3.2. Parameter uncertainties considered

Following case 1 and 2 of Table 3 in Ref. [30], two cases of uncertainty are considered. However, the parameter uncertainty is modeled as Eqs. (13) and (14). The parameter uncertainty bounds are listed in Table 5.

### 3.3.3. Numerical results

In the following, the combined effects of parameter uncertainties and faults on the peak vibration response are investigated using the proposed method. The norm of the Fourier coefficients  $\mathbf{U}$  of the translation displacements is to be maximized. The two excitation frequencies  $\omega_r$  and  $\omega_b$  are considered as optimization variables. Optimizations are then performed and the optimization results for the two cases are shown in Table 2 where case 0 corresponds to the worst resonance response of the deterministic system, which is taken as a reference solution for comparison.

From Table 6, it can easily find that the resonance frequencies remain almost unchanged for the three cases and are very close to the first critical speed of the deterministic system. For cases 1 and 2 the worst case configuration corresponds to  $v_E = 0$  and  $v_{U_0} = 1$  while the uncertainty variables  $v_m$  and  $v_h$  for case 2 are both equal to 1.

The whirl orbit is one of the most important features for representing the motion stable. The orbits of the rotor system are plotted in Fig. 12 for node 7 where the highest vibration amplitudes are expected to appear. The portraits of node 7 in the  $x$  and  $y$  directions for the 3 cases are shown in Fig. 13 where the left figures represent the portraits in the  $x$  direction and the portraits in the  $y$  direction correspond to the right figures. Observe in Figs. 12 and 13 that the overall response in these 3 cases is similar and the major differences are in their magnitude. The worst resonance response amplitude for case 0 is 0.0127 (m) and the worst resonance response amplitude for case 1 is about 0.01376542 (m). The worst resonance response amplitude for case 1 is slightly higher than that for case 0. It is noticeable that the effect of varying  $v_E$  and  $v_{U_0}$  is small. The resonance response level for case 2 has its maximum value 0.01378769 (m). In comparison with case 1 the worst resonance response for case 2 is insensitive to variation of  $v_m$  and  $v_h$ .

The frequency contents for the 3 cases are plotted in Fig. 14. For the rotor system with support excitation, it is shown in Fig. 14 that for the three cases, the response spectrum shows no significant change and the dominant harmonic component of the worst case resonance response is the support excitation frequency. Although frequencies equal to the combination of support excitation frequency and single rotating speed are found in the response spectrum (particular in the  $x$  direction), however, only the harmonic component around the support excitation frequency has significant contribution.

In order to get the statistic characteristics of the vibration peak response, Monte Carlo simulations are often used. In the Monte Carlo simulations, many samples of the uncertainty variables are needed. For each sample with fixed the uncertainty variables, the resonance peak response is obtained by sweeping the two dimensional excitation frequencies. Firstly, a scanning calculation of  $\omega_b$  with  $\omega_r$  at a constant value is carried out to find the maximum vibration response. Then, the resonance peak response is retrieved via another scanning calculation of  $\omega_r$ . The computational cost of the two dimensional frequency sweeping is expensive. In addition, the more the number of uncertainty variables is considered, the more the number of samples is needed, thus leading to the Monte Carlo simulations difficult to perform. On the contrary, only one optimization effort is performed to get the worst vibration response to quantify the response bound. The advantage of the developed method is obvious.

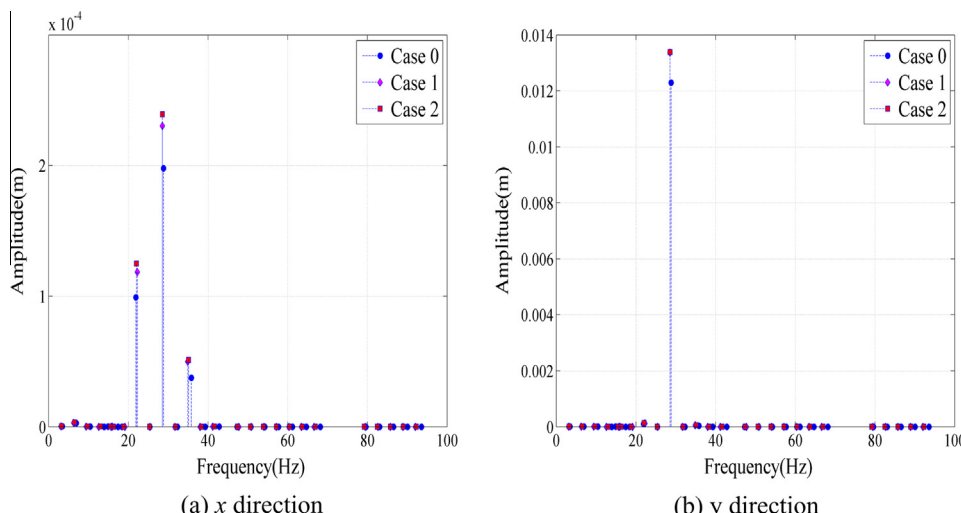


**Fig. 14.** The frequency spectrums of node 7 in the  $x$  and  $y$  directions for the three cases.

#### 4. Conclusions

A novel method for the numerical prediction of the quasi periodic motions of nonlinear mechanical systems has been developed. The method is essentially a nonlinear constrained optimization problem and consists of a two-step procedure: In the first step, the multi-dimensional harmonic balance method is performed to directly construct the nonlinear equality constraints. In the second step, the MultiStart optimization algorithm is used to find the optimization solution. The proposed methodology is applied to several nonlinear mechanical systems ranging from single degree-of-freedom to finite element rotor models. It is illustrated that the proposed approach can be used to find the worst resonant response and the upper and lower response bounds of quasi-periodic solution and is also able to quantify the combined influences of structural uncertainties and non-regular nonlinearities on the nonlinear quasi-periodic vibrations of nonlinear systems.

For further researches, the proposed method will be used to deal with the parametric systems which are frequently used in gear boxes and vehicle motions [31][32]. Using the proposed method, the global (worst) resonance response of the parametric systems can be obtained. In addition, the stability analysis is an important research content of the parametric systems. The stability analysis problem is transform into a generalized eigenvalue problem. Using the Floquet theory, the bifurcation condition can be set as the object function to analyze the stability boundary. When considering the parameter uncertainty, an interval eigenvalue problem for the stability analysis can be solved using the interval analysis method. The stability boundary is determined by the interval eigenvalue. Another paper on the parametric systems will be reported in future study.

For the problem in Ref. [33], the following matrix differential equation (see Eq. (6) in Ref. [33]) is considered:

$$\mathbf{C}\dot{\delta} + \mathbf{K}\delta + \mathbf{f}_{nl}(\delta) = \mathbf{p}(t) \quad (19)$$

With

$$\begin{aligned} \mathbf{C} &= \iint \mathbf{N}^T \rho \mathbf{N} dx dy, \quad \mathbf{K} = \iint \mathbf{B}^T \mu_1 \mathbf{B} dx dy + \oint \mathbf{M}^T \alpha \mathbf{M} ds \\ \mathbf{f}_{nl}(\delta) &= \iint \mathbf{B}^T \mu_2 \sqrt{\left(\frac{\partial w}{\partial x}\right)^2 - \left(\frac{\partial w}{\partial y}\right)^2} \mathbf{B} \delta dx dy, \quad \mathbf{p}(t) = \iint \mathbf{N}^T \left( \rho g - \frac{\partial p}{\partial z} \right) dx dy + \oint \mathbf{M}^T \alpha w^* ds \end{aligned}$$

where  $\mathbf{f}_{nl}(\delta) = \iint \mathbf{B}^T \mu_2 \sqrt{\left(\frac{\partial w}{\partial x}\right)^2 - \left(\frac{\partial w}{\partial y}\right)^2} \mathbf{B} \delta dx dy$  is a nonlinear function of the nodal velocity vector  $\delta$  and is taken as the nonlinear forcing  $\mathbf{f}_{nl}$  in Eq. (1). In the following, the process for solving Eq. (19) is formulated. Firstly, the nodal velocity vector  $\delta$  is expressed as a finite Fourier series similar to Eq. (2). Then, utilizing the harmonic balance principle, a set of nonlinear algebraic equations is obtained by substituting Eq. (2) into Eq. (19). This set of nonlinear algebraic equations is taken as the nonlinear equality constraints in Eq. (8). Finally, the Fourier coefficients of  $\delta$  are set as the optimization variables in Eq. (8) and are solved iteratively by the OQNLP MultiStart optimization algorithm. The effects of excitation frequency on the mass flow rate and the relationship between the mass flow rate and the excitation amplitude can also be revealed by using the proposed method. In addition, with the help of the Floquet theory the stability (or instability) regions of the harmonic motion can be obtained. Another paper about the example in Ref. [33] will be considered.

#### Acknowledgements

The author is grateful to the anonymous referees for their valuable comments. This study has been financially supported by Natural Science Foundation of China (Project No. 10904178).

#### Appendix A

After derivation, the element matrices are given as follows:

$$K_0^e = \frac{EI_m}{l^3} \begin{bmatrix} 12 & 0 & 0 & -6l & -12 & 0 & 0 & -6l \\ 12 & 6l & 0 & 0 & -12 & 6l & 0 & 0 \\ 4l^2 & 0 & 0 & -6l & 2l^2 & 0 & 0 & 0 \\ & 4l^2 & 6l & 0 & 0 & 2l^2 & 0 & 0 \\ & & 12 & 0 & 0 & 6l & 0 & 0 \\ \text{Sym} & & & 12 & -6l & 0 & 0 & 0 \\ & & & & 4l^2 & 0 & 0 & 0 \\ & & & & & 4l^2 & 0 & 0 \end{bmatrix} \quad (A-1)$$

$$K_c^e = \frac{EI_d}{l^3} \begin{bmatrix} 12 & 0 & 0 & -6l & -12 & 0 & 0 & -6l \\ -12 & -6l & 0 & 0 & 12 & -6l & 0 & 0 \\ & -4l^2 & 0 & 0 & 6l & -2l^2 & 0 & \\ & & 4l^2 & 6l & 0 & 0 & 2l^2 & \\ & & & 12 & 0 & 0 & 6l & \\ & & \text{Sym} & & -12 & 6l & 0 & \\ & & & & -4l^2 & 0 & & \\ & & & & & 4l^2 & & \end{bmatrix} \quad (\text{A-2})$$

$$K_s^e = \frac{EI_d}{l^3} \begin{bmatrix} 0 & -12 & -6l & 0 & 0 & 12 & -6l & 0 \\ 0 & 0 & 6l & 12 & 0 & 0 & 6l & \\ 0 & 4l^2 & 6l & 0 & 0 & 0 & 2l^2 & \\ 0 & 0 & -6l & 2l^2 & 0 & & & \\ 0 & -12 & 6l & 0 & & & & \\ \text{Sym} & & 0 & 0 & -6l & & & \\ & & & 0 & -4l^2 & & & \\ & & & & 0 & & & \end{bmatrix} \quad (\text{A-3})$$

$$G^e = \frac{\rho I_m}{15l} \begin{bmatrix} 0 & -36 & -3l & 0 & 0 & 36 & -3l & 0 \\ 0 & 0 & -3l & -36 & 0 & 0 & 0 & -3l \\ 0 & -4l^2 & -3l & 0 & 0 & 0 & l^2 & \\ 0 & 0 & -3l & -l^2 & 0 & & & \\ 0 & -36 & 3l & 0 & & & & \\ \text{Sym} & & 0 & 0 & 3l & & & \\ & & & 0 & -4l^2 & & & \\ & & & & 0 & & & \end{bmatrix} \quad (\text{A-4})$$

$$Mt_0^e = \frac{\rho Sl}{420} \begin{bmatrix} 156 & -12 & -6l & 0 & 0 & 12 & -6l & 0 \\ 156 & 22l & 0 & 0 & 54 & -13l & 0 & \\ 4l^2 & 0 & 0 & 13l & -3l^2 & 0 & & \\ 4l^2 & -13l & 0 & 0 & 0 & -3l^2 & \\ 156 & 0 & 0 & 0 & 22l & & & \\ \text{Sym} & & 156 & -22l & 0 & & & \\ & & & 4l^2 & 0 & & & \\ & & & & 4l^2 & & & \end{bmatrix} \quad (\text{A-5})$$

$$Mr_0^e = \frac{\rho I_m}{30l} \begin{bmatrix} 36 & 0 & 0 & -3l & -36 & 0 & 0 & -3l \\ 36 & 3l & 0 & 0 & -36 & 3l & 0 & \\ 4l^2 & 0 & 0 & -3l & -l^2 & 0 & & \\ 4l^2 & 3l & 0 & 0 & 0 & -l^2 & \\ 36 & 0 & 0 & 0 & 3l & & & \\ \text{Sym} & & 36 & -3l & 0 & & & \\ & & & 4l^2 & 0 & & & \\ & & & & 4l^2 & & & \end{bmatrix} \quad (\text{A-6})$$

$$M_c^e = \frac{\rho I_d}{30l} \begin{bmatrix} 36 & 0 & 0 & -3l & -36 & 0 & 0 & -3l \\ -36 & -3l & 0 & 0 & 36 & -3l & 0 & 0 \\ 0 & -4l^2 & 0 & 0 & 3l & l^2 & 0 & 0 \\ 0 & 4l^2 & 3l & 0 & 0 & 0 & -l^2 & 0 \\ 0 & 36 & 0 & 0 & 3l & 0 & 0 & 3l \\ 0 & 0 & Sym & -36 & 3l & 0 & -4l^2 & 0 \\ 0 & 0 & 0 & -4l^2 & 0 & 0 & 4l^2 & 0 \\ 0 & 0 & 0 & 0 & 0 & 0 & 0 & 0 \end{bmatrix} \quad (\text{A-7})$$

$$M_s^e = \frac{\rho I_d}{30l} \begin{bmatrix} 0 & -36 & -3l & 0 & 0 & 36 & -3l & 0 \\ 0 & 0 & 3l & 36 & 0 & 0 & 3l & 0 \\ 0 & 0 & 4l^2 & 3l & 0 & 0 & -l^2 & 0 \\ 0 & 0 & 0 & -3l & -l^2 & 0 & 0 & 0 \\ 0 & 0 & 0 & -36 & 3l & 0 & 0 & 0 \\ 0 & 0 & Sym & 0 & 0 & -3l & 0 & 0 \\ 0 & 0 & 0 & 0 & 0 & 4l^2 & 0 & 0 \end{bmatrix} \quad (\text{A-8})$$

## References

- [1] Lau SL, Cheung YK. Amplitude incremental variational principle for nonlinear vibration of elastic systems. *J Appl Mech* 1981;48:959–64.
- [2] Cameron TM, Griffin JH. An alternating frequency/time domain method for calculating the steady-state response of nonlinear dynamic systems. *J Appl Mech* 1989;56(1):149–54.
- [3] Nacivet S, Pierre C, Thouverez F, et al. A dynamic Lagrangian frequency–time method for the vibration of dry-friction-damped systems. *J Sound Vib* 2003;265(1):201–19.
- [4] Laxalde D, Thouverez F, Sinou JJ, et al. Qualitative analysis of forced response of blisks with friction ring dampers. *Eur J Mech A Solids* 2007;26(4):676–87.
- [5] Hall KC, Thomas JP, Clark WS. Computation of unsteady nonlinear flows in cascades using a harmonic balance technique. *AIAA J* 2002;40(5):879–86.
- [6] Liu L, Dowell EH, Thomas JP. A high dimensional harmonic balance approach for an aeroelastic airfoil with cubic restoring forces. *J Fluids Struct* 2007;23(3):351–63.
- [7] Liu L, Thomas JP, Dowell EH, et al. A comparison of classical and high dimensional harmonic balance approaches for a Duffing oscillator. *J Comput Phys* 2006;215(1):298–320.
- [8] LaBryer A, Attar PJ. High dimensional harmonic balance dealiasing techniques for a Duffing oscillator. *J Sound Vib* 2009;324(3):1016–38.
- [9] Coelhin B, Vergez C. A high order purely frequency-based harmonic balance formulation for continuation of periodic solutions. *J Sound Vib* 2009;324(1):243–62.
- [10] Sarrouy E, Dessimoz O, Sinou JJ. Stochastic study of a non-linear self-excited system with friction. *Eur J Mech A Solids* 2013;40:1–10.
- [11] Jaumouillé V, Sinou JJ, Petitjean B. An adaptive harmonic balance method for predicting the nonlinear dynamic responses of mechanical systems—Application to bolted structures. *J Sound Vib* 2010;329(19):4048–67.
- [12] Sarrouy E, Thouverez F. Global search of non-linear systems periodic solutions: a rotordynamics application. *Mech Syst Sig Process* 2010;24(6):1799–813.
- [13] Alexander NA. Estimating the nonlinear resonant frequency of a single pile in nonlinear soil. *J Sound Vib* 2010;329(8):1137–53.
- [14] Chua L, Ushida A. Algorithms for computing almost periodic steady-state response of nonlinear systems to multiple input frequencies. *Circuits Syst* 1981;28(10):953–71.
- [15] Lau SL, Cheung YK. Incremental harmonic balance method with multiple time scales for aperiodic vibration of nonlinear systems. *J Appl Mech* 1983;50:871–6.
- [16] Pušenjak RR, Oblak MM. Incremental harmonic balance method with multiple time variables for dynamical systems with cubic non-linearities. *Int J Numer Methods Eng* 2004;59(2):255–92.
- [17] Kim YB, Noah ST. Quasi-periodic response and stability analysis for a non-linear Jeffcott rotor. *J Sound Vib* 1996;190(2):239–53.
- [18] Kim YB, Choi SK. A multiple harmonic balance method for the internal resonant vibration of a non-linear Jeffcott rotor. *J Sound Vib* 1997;208(5):745–61.
- [19] Guskov M, Sinou JJ, Thouverez F. Multi-dimensional harmonic balance applied to rotor dynamics. *Mech Res Commun* 2008;35(8):537–45.
- [20] Guskov M, Thouverez F. Harmonic balance-based approach for quasi-periodic motions and stability analysis. *J Vib Acoust* 2012;134(3):031003-1–031003-11.
- [21] Sinou JJ, Faverjon B. The vibration signature of chordal cracks in a rotor system including uncertainties. *J Sound Vib* 2012;331(1):138–54.
- [22] Didier J, Sinou JJ, Faverjon B. Study of the non-linear dynamic response of a rotor system with faults and uncertainties. *J Sound Vib* 2012;331:671–703.
- [23] Didier J, Sinou JJ, Faverjon B. Nonlinear vibrations of a mechanical system with non-regular nonlinearities and uncertainties. *Commun Nonlinear Sci Numer Simul* 2013;18:3250–70.
- [24] Millman DR, King PI, Beran PS. Airfoil pitch-and-plunge bifurcation behavior with Fourier chaos expansions. *J Aircr* 2005;42(2):376–84.
- [25] Moens D, Vandepitte D. A survey of non-probabilistic uncertainty treatment in finite element analysis. *Comput Method Appl Mech Eng* 2005;194(12):1527–55.
- [26] Wu J, Zhang Y, Chen L, et al. A Chebyshev interval method for nonlinear dynamic systems under uncertainty. *Appl Math Modell* 2013;37(6):4578–91.
- [27] Ugray Z, Lasdon L, Plummer J, et al. Scatter search and local NLP solvers: a multistart framework for global optimization. *INFORMS J Comput* 2007;19(3):328–40.

- [28] Nocedal J, Wright S. Numerical optimization, series in operations research and financial engineering. New York: Springer; 2006.
- [29] Fletcher R. Practical methods of optimization. John Wiley & Sons; 2013.
- [30] Didier J, Sinou JJ, Faverjon B. Multi-dimensional harmonic balance with uncertainties applied to rotor dynamics. *J Vib Acoust* 2012;134:061003-1–061003-17.
- [31] Warminski J, Litak G, Szabelski K. Synchronisation and chaos in a parametrically and self-excited system with two degrees of freedom. *Nonlinear Dyn* 2000;22:125–43.
- [32] Borowiec M, Litak G. Transition to chaos and escape phenomenon in two-degrees-of-freedom oscillator with a kinematic excitation. *Nonlinear Dyn* 2012;70:1125–33.
- [33] Ragulskis M, Fedaravicius A, Ragulskis K. Harmonic balance method for FEM analysis of fluid flow in a vibrating pipe. *Commun Numer Methods Eng* 2006;22(5):347–56.